Lowland Technology International 2018; 20 (3): 273-284
International Association of Lowland Technology (IALT): ISSN 1344-9656

Research Paper

Characteristics of the second stage of evaporation and water redistribution through double layered sandy soil profiles

A. Alowaisy [1] and N. Yasufuku [2]

ARTICLE INFORMATION

Article history:

Received: 23 April, 2018
Received in revised form: 22 August, 2018
Accepted: 07 September, 2018
Publish on: 07 December, 2018

Keywords:

Actual evaporation
Water storage
Double layered soil profile
Water redistribution
Drying front depth

ABSTRACT

Evaporation from porous media involves a complex pore scale water and vapor transportation that directly affects the liquid phase distribution and fluxes. The presence of textural contrast boundary in multilayered profiles adds to the complexity. This study aims at evaluating the textural contrast boundary depth and individual layer thickness influence on the actual evaporation and water storage through double-layered soil profiles. For coarse overlying fine sand, it was found that the top layer small capillaries contribute to the majority of water lost through the falling rate stage. Considering fine overlying coarse sand profiles, the pumping phenomenon from the bottom coarse layer to the top fine layer occurs before the arrival of the drying front to the textural boundary due to the increasing suction forces within the top fine layer. The water storage capability of double layered soil profiles depends highly on the top to the bottom small capillaries ratio multiplied by the layer thickness ratio. Regardless the atmospheric conditions and layering sequence, it was concluded that the shallower the textural contrast boundary results in decreasing the total duration required to achieve the residual evaporation stage thus leads to higher water storage capabilities through the first and second evaporation stages.

1. Introduction

Evaporation from porous media is an essential process that involves water and vapor mass exchange between land and atmosphere. It varies considerably with time and space due to the complex interaction between internal flow fluxes (thermal and hydraulic conductivities and vapor diffusion) and atmospheric demand (humidity, temperature and velocity of ambient air) (Brutsaert, 2005). Van Brakel (1980) and Prat (2002) highlighted the complexity of the interactions between medium properties, transport processes and boundary conditions which result in a wide range of evaporation behaviors that are difficult to predict.

Evaporation plays an important role in various engineering, environmental and hydrological aspects. It is essential for many geotechnical and geo-environmental problems such as design of soil cover systems in mine reclamation (Yanful et al., 1993; Aubertin et al., 1996), prediction of expansive soil behavior, evaluation of pore pressure in natural slopes or man-made embankments, water resources management and so on (Wilson et al., 1994; Murakami et al., 2002; Blight, 2002, 2003; Yanful et al., 2003).

---

[1] Graduate student, Geotechnical Engineering Laboratory, Department of Civil and Structural Engineering, Faculty of Engineering, Kyushu University, 744 Motooka, Nishi-ku, Fukuoka 819-0395, JAPAN, adel_owaisi@yahoo.com
[2] Professor, Geotechnical Engineering Laboratory, Department of Civil and Structural Engineering, Faculty of Engineering, Kyushu University, 744 Motooka, Nishi-ku, Fukuoka 819-0395, JAPAN, yasufuku@civil.kyushu-u.ac.jp
Note: Discussion on this paper is open until June 2019

The extreme evaporation of soil water induces generation of salt efflorescence and soil crusts and significantly affects the vegetation cover which in turn causes serious environmental degradation and extreme drought conditions. Where under such extreme conditions, wind easily mobilize dust from these surfaces (Gillette et al., 2001). Dust production is considered as a major environmental concern, where the particulate matter impacts air quality and human health (Schwartz, 1994).

The evaporation process involves two main distinct stages: constant rate stage (SI) and falling rate stage, mainly divided into two sub-stages: Falling rate stage (SII) and Residual stage (SIII) (Fisher, 1923). SI lasts as long as the drying front remains hydraulically connected to the soil surface where water molecules vaporize and get lost into the overlying air layer (Yiotis et al., 2006; Lehmann et al., 2008). As the hydraulic conductivity of the soil decreases with the desaturation of the soil, the hydraulic connection to the soil surface gets lost and thus identifies the beginning of SII governed by vapor diffusion through the porous medium (Prat, 2002; Shokri et al., 2008; Shahraeeni et al., 2012). Especially in arid and semi-arid regions, most of water loss occurs during SII, where SI lasts only for short time after rainfall or irrigation events (Brutsaert and Chen, 1995).

Lehmann et al. (2008) proposed the intrinsic characteristic length concept that can be deduced from the pore size distribution of the soil medium. It is a measure of the distance over which hydraulic continuity can be maintained considering balance between gravitational, capillary and viscous forces. It was concluded that when the drying front which is defined as the equivalent distance between the evaporating surface and drying front position exceeds the characteristic length, the small capillaries liquid menisci start retreating below the evaporating surface which interrupts liquid continuity to the surface indicating the beginning of SII.

Shahraeeni et al. (2012) studied the surface boundary conditions in link to the internal mechanism of mass transport and elaborated the evolution of the surface water dynamics and its impact on the macroscopic evaporation through the first stage of evaporation. The study revealed that for large ratios of boundary layer thickness (δ) to pore size [radius (r)], the relative evaporation rate (ratio of evaporation from porous surface to evaporation from free water under similar conditions) remains almost constant even when the surface water content is reduced to nearly its residual value. Considering evaporation from small pores into a thick boundary layer (large δ/r ratio), the vapor diffusion field evolves from nearly 1-D stratified structure for the initially wet surface to a collection of 3-D individual vapor shells that form over discrete pores as the surface dries and spacing between active pores increases. These changes in diffusion field configuration result in significant increase in vapor flux per pore that may fully compensate for the reduced evaporating area.

Diaz et al. (2005) indicated in an experimental study considering evaporation from various thicknesses of volcanic mulch layer overlying silty clay layer that regardless the thickness and grain size of the mulch layer, evaporation from the covered soil was lower than the uncovered soil.

The effect of layer sequence on evaporation behavior in two-layer porous profiles was investigated by Pillai et al. (2009) using the pore network model. Simulation results showed that layer sequence significantly affects the liquid phase distribution patterns and evaporation rates. It was indicated that preferential water loss occurred for small pores soil overlying large pores soil. On the other hand, for a reversed sequence, air invades the underlying fine layer after the top coarse layer achieved zero saturation.

The characteristic length proposed by Lehmann et al. (2008) was extended considering layered porous media. The proposed composite characteristic length (Shokri et al., 2010) indicates the drying front depth at the end of SI evaporation. It was demonstrated that air ingress into the interface between fine and coarse sand layers resulting in a capillary pressure jump and subsequent relaxation that significantly modify liquid phase distribution. For fine overlying coarse sand layers, rapid and disproportionate water displacement ejecting water to the upper fine layer as a result of the introduced pressure was observed. This indicates that water distribution through layered soil profiles is significantly different and more complicated compared to the homogeneous soil profiles.

Most of the existing studies consider evaluating the evaporation from multilayered soil profiles without considering the role of controlling the textural layering on the actual evaporation rate and water redistribution within each layer. This study aims at evaluating the textural contrast boundary depth and individual layer thickness influence on the actual evaporation rate and water storage through double-layered soil profiles. In addition, the evaporation dynamics considering the influence of the textural contrast boundary presence on the vapor diffusion and the receding front depth through the falling evaporation rate stage are elaborated.

2. Materials and methodology

2.1 Materials

Tests were conducted using silica sand that is resistant to volume change during desiccation. Thus the shrinkage and cracking effect can be neglected. Two texturally distinct silica sand provided by Kumamoto-Silica Mining Co., Ltd, Japan soils were used: 1) K-7 (fine silica sand) and 2) K-4 (coarse silica sand). Summary of the soil properties and the particle size distribution curves are shown in **Table 1** and **Fig. 1** respectively.

Water retention curves (WRC) for the two tested soils were determined using the axis translation pressure plate cells (Tempe cells). The obtained results were then fitted with Van Genuchten model (Van Genuchten, 1980) as depicted in **Fig. 2**. The fitting parameters of Van Genuchten model for the fine and coarse sands are presented in **Table 1**.

2.2 Experimental setup

A simple experimental setup was adopted which considers repeatability, low cost and accurate continuous measuring of the evaporation rate and water redistribution through soil profiles. As demonstrated in **Fig. 3**, columns were constructed using a 10.4 cm in diameter acrylic material with wall thickness of 0.5 cm. Columns then were attached to porous plate in order to uniformly distribute the water to the whole soil profile and then the base circumference was sealed properly to prevent water leakage. A valve was installed to the base for saturation purposes. Each column was instrumented with moisture sensors installed through drilled ports which allow continuous measuring of the water distribution through the entire soil profile. Ports were sealed properly using silicon paste in order to prevent water leakage.

The actual evaporation rate from each column was continuously obtained by independently measuring the mass of each column using a balance with 31kg capacity and ±1 g resolution. Each balance was connected to a weighing data logger for continuous recording of the columns masses. The potential evaporation rate was measured using an evaporation pan placed adjacent to the soil columns and subjected to the same testing conditions. The pan was frequently replenished in order to keep the water surface at the same level as the columns surfaces.

Teng et al. (2014) mentioned that higher temperature and higher wind speed leads to higher evaporation rate and thus accelerates the testing process. Based on that, in order to decrease the testing period by increasing the evaporation rate, a 250-watt heater lamp in addition to a fan with 102 m/min. wind speed were installed above the soil surface of each column as depicted in **Fig. 3**. A Hygro-thermometer was installed 15 cm above the experimental setup which allows continuous recording of the relative humidity and temperature of the experimental zone.

2.3 Soil columns preparation

Several sandy soil placement methods were reported in literature such as pluviation, vibration and tamping. A single layer of filter paper was placed on the porous plate

Table 1. Adopted silica sand physical and hydrological properties. Water retention curve fitted with Van Genuchten model (1980) are shown in the hydrological properties section. K-7 and K-4 charachteristc length based on Lehmann et al. (2008) are indicated.

Physical properties	K-7	K-4
Specific gravity [GS]	2.642	2.640
Dry density (g/cm^3) [ρ_s]	1.618	1.552
Coarse sand (%)	0.0	19.5
Medium sand (%)	10.0	80.5
Fine sand (%)	74.6	0.0
Silt (%)	15.4	0.0
Uniformity coefficient [Uc]	2.966	1.238
Curvature coefficient [Uc`]	1.395	0.969
Median diameter (mm) [D50]	0.161	0.740
Hydrological properties		
k_s (ms^{-1})	1.14 x10^{-5}	2.07x10^{-3}
θ_s, Saturated water content (cm^3 cm^{-3})	0.420060	0.425400
θ_r, Residual water content (cm^3 cm^{-3})	0.075373	0.028457
α (cm^{-1})	0.011775	0.075720
n	10.448	3.194
Characteristics length (L_i) (mm)	179	117

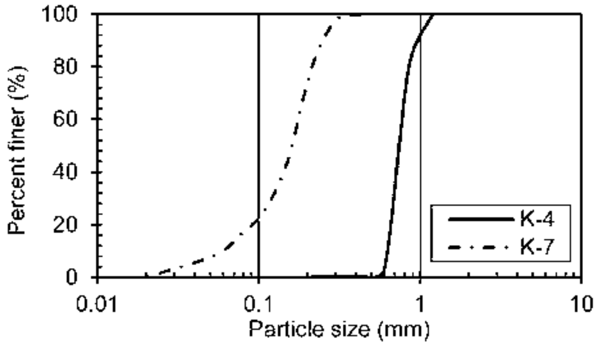

Fig. 1. Particle size distribution curve for K-4 (coarse silica sand) and K-7 (fine silica sand).

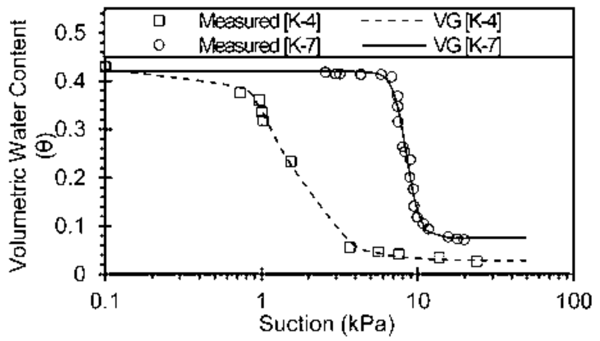

Fig. 2. Soil water retention curves. Results were obtained using the axis translation pressure plate cells (Tempe cells) indicated by the scatter plot. Results were then fitted with Van Genuchten model (1980) indicated by the solid and dashed lines for K-7 and K-4 silica sands respectively. The fitting parameters of Van Genuchten model are listed in **Table 1**.

in order to prevent soil from blocking the pores and to uniformly distribute water to the soil bottom. Soil was filled in separated layers and compacted to the maximum dry density, where all the layers were placed using identical placement techniques following the standard Japanese testing method (JIS 1224) for determining the maximum dry density of sandy soil. Moisture sensors were installed carefully during the placement of sand layers. The columns were filled in lifts of 3-6 cm and tapped with rubber hammer to disturb the soil in order to obtain consistent and uniform densities. After installing the top soil layer, the surface was trimmed to be level with the top of the column. Then the moisture sensor ports were sealed properly in order to prevent water leakage.

A constant water head was applied to the columns through the water inlet valve in the base. The water supply was kept till the columns achieved fully saturation through the entire soil profile. Then the water valves were closed and the water head was removed.

2.4 *Testing procedure*

In this study, 12 fine overlying coarse and coarse overlying fine sand double layered column configurations were adopted. Through the whole testing period the evaporation rate, saturation profile, relative humidity and temperature were continuously measured with a constant interval of 15 minutes. The evaporation tests were shut down when the evaporation rate of all columns achieved SIII where the evaporation rate becomes low and stable. **Table 2** illustrates the adopted configurations, layering sequences, thicknesses and the corresponding composite characteristic length as defined by Lehmann et al. (2008) and Shokri et al. (2010). In addition, the average temperature (c°), average Relative Humidity [RH] (%) and the average potential evaporation within the testing zone are also depicted.

Following Lehmann et al. (2008), the characteristic length (L_c) for coarse and fine sands are determined by linearizing the WRC shown in **Fig. 2**.

$$L_C = \frac{2\sigma}{\rho g}\left(\frac{1}{r1} - \frac{1}{r2}\right) \qquad [1]$$

where σ is the water-air surface tension; ρ is the water density; g is the acceleration of gravity; r_1 is the smallest drainable pore; r_2 is the largest drainable pore.

$$r_1 = \frac{2\sigma}{\rho g(h_b + \Delta h_{cap})} \qquad [2]$$

$$r_2 = \frac{2\sigma}{\rho g}\alpha \qquad [3]$$

$$\Delta h_{cap} = L_G = \frac{1}{\alpha(n-1)}\left(\frac{2n-1}{n}\right)^{\frac{2n-1}{n}}\left(\frac{n-1}{n}\right)^{\frac{1-n}{n}} \qquad [4]$$

No.	Accessory	Functions and remarks
1	Soil column	Acrylic material, Diameter: 10.4 cm, wall thickness: 0.5cm, height [30, 40, 50] cm
2	Water valve	For saturation purposes
3	Scale	GP-32K, AND Co. Ltd, 0.1g solution
4	Water content sensors	EC-5 soil moisture sensors
5	Heater lamp	250 watt, to accelerate the evaporation tests
6	Air blender (Fan)	Wind speed 102 m/min., to rabble the air.
7	Humidity/Temperatures monitor	MHT – 381SD, humidity and temperature continuous monitoring
8,9	Data loggers	Continuous data acquisition

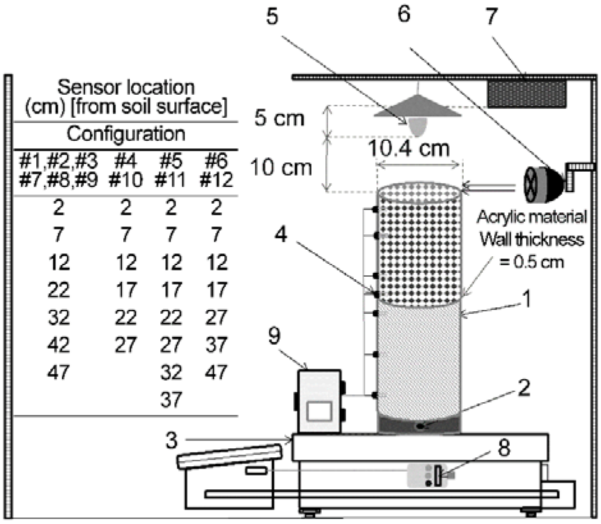

Sensor location (cm) [from soil surface]

Configuration			
#1,#2,#3 #7,#8,#9	#4 #10	#5 #11	#6 #12
2	2	2	2
7	7	7	7
12	12	12	12
22	17	17	17
32	22	22	27
42	27	27	37
47		32	47
		37	

Fig. 3. Experimental setup. Columns were constructed using a 10.4 cm in diameter acrylic material with wall thickness of 0.5 cm. The actual evaporation rate from each column was continuously obtained by independently measuring the mass of each column. Water redistribution was measured using moisture sensors installed through the soil profile. A heater lamp in addition to a fan were installed at the top of the surface to accelerate the testing process. A Hygro-thermometer was used to continuous measuring the temperature and relative humidity.

Table 2. Adopted configurations and atmospheric. Adopted configurations numbers, layering sequences, testing duration and average (Temperature, Relative humidity and Potential evaporation). C: coarse silica sand. F: fine silica sand.

Group	C/F		F/C	
	(1)	(2)	(3)	(4)
	#(1, 2, 3)	#(4,5, 6)	#(7, 8, 9)	#(10,11, 12)
$\frac{\text{Top(cm)}}{\text{Bottom (cm)}}$	$\frac{5}{45},\frac{15}{35},\frac{25}{25}$	$\frac{5,15,25}{25}$	$\frac{5}{45},\frac{15}{35},\frac{25}{25}$	$\frac{5,15,25}{25}$
[L_c] (mm)	50, 117, 117		167, 267, 179	
Temperature average	30.98 (c°)	30.72(c°)	21.67 (c°)	27.89 (c°)
RH average (%)	59.63	61.30	65.76	60.36
Average [E_P] (mm/hr.)	2.54	3.35	2.45	3.06
Duration (hrs.)	286.5	286.5	286.5	286.5

L_c: Composite characteristics length defined as the drying front depth at the end of SI (onset of SII).

$$h_b = \frac{1}{\alpha}\left(\frac{n-1}{n}\right)^{\frac{1-2n}{n}} - \Delta h_{cap} \qquad [5]$$

Where Δh_{cap} is the capillary head difference; h_b is the air entry value; α and n are the Van Genuchten fitting parameters where n is a measure of the pore-size distribution and α is related to the inverse of the air entry suction value.

The end of SI is indicated by determining the composite characteristic length (L_c) as indicated by Shokri et al. (2010) following the algorithm shown in **Fig. 4**.

The drying front depth was determined assuming a linear decrease of water content from drying front to the surface as recommended by Lehmann et al. (2008). Thus the evaporation front depth can be calculated as follows:

$$FD = \frac{1}{2}(\Phi - \theta)Lc \qquad [6]$$

where ϕ is the porosity.

3. Results and discussion

3.1 Coarse overlying fine sand profiles

3.1.1 Evaporation rate and drying front depth

In total six coarse overlying fine soil configurations divided into two groups were adopted as mentioned in **Table 2**. Through the first group, the depth of the textural contrast boundary was investigated by changing the top to the bottom layer thickness ratio [top and bottom layer thicknesses vary (#1, #2 and #3)], while for the second group the depth of the textural contrast boundary was investigated by changing the top coarse sand layer thickness while the bottom fine sand layer thickness maintained constant through the three adopted configurations (#4, #5 and #6). Adopted configurations were subjected to the same testing conditions within the same group.

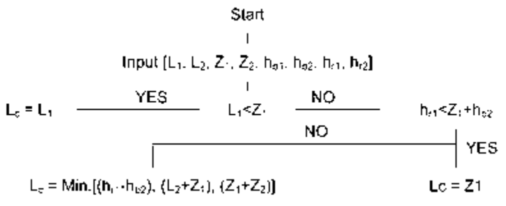

Fig. 4. Composite characteristic length. The algorithm for calculating the composite characteristic length for double layered soil profiles. L_c is the composite characteristic length; L_i is the individual layer characteristic length; Z_i is the layer thickness; h_{ri} is the suction at residual water content; h_{bi} is the air entry value.

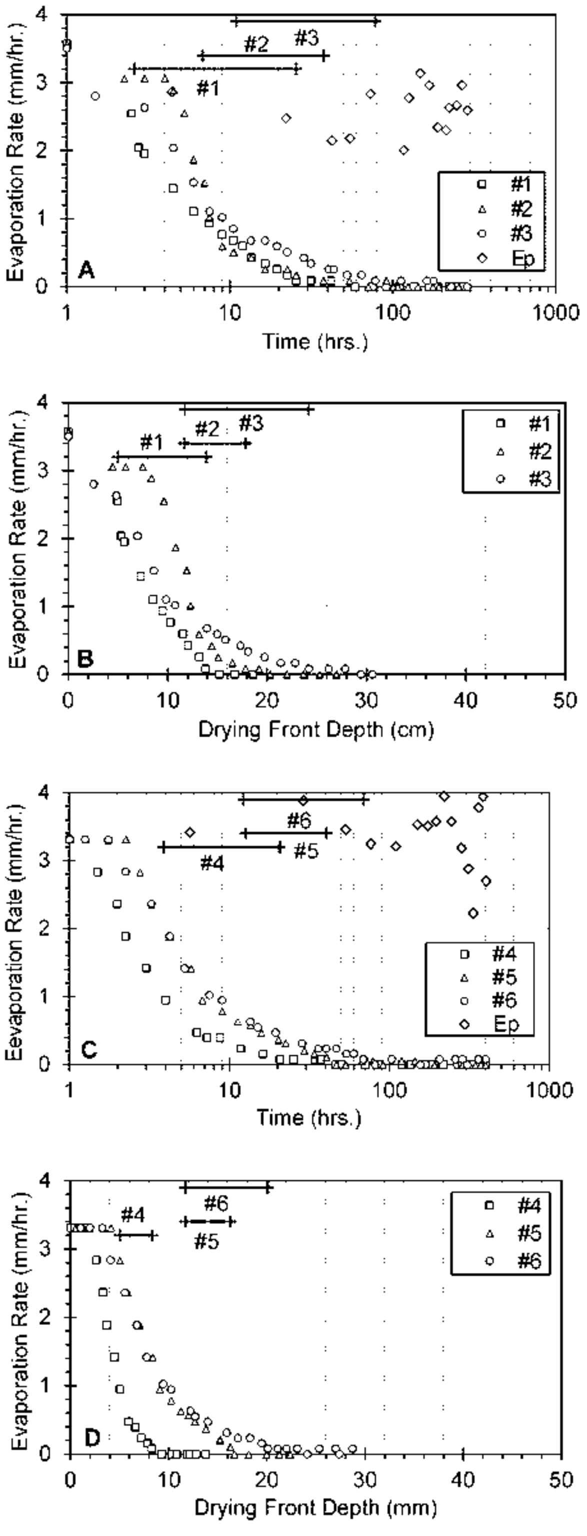

Fig. 5. Actual evaporation rates for coarse overlying fine sand adopted configurations through groups 1 and 2. A and B show the evaporation rate versus time and drying front depth for group 1 (#1, #2 and #3 adopted configurations) respectively. C and D demonstrate the evaporation rate versus time and drying front depth for group 2 (#4, #5 and #6 adopted configurations) respectively. The potential evaporation rate obtained by an evaporation pan placed adjacent to the soil columns and subjected to the same testing conditions is also shown in Figs. A and C.

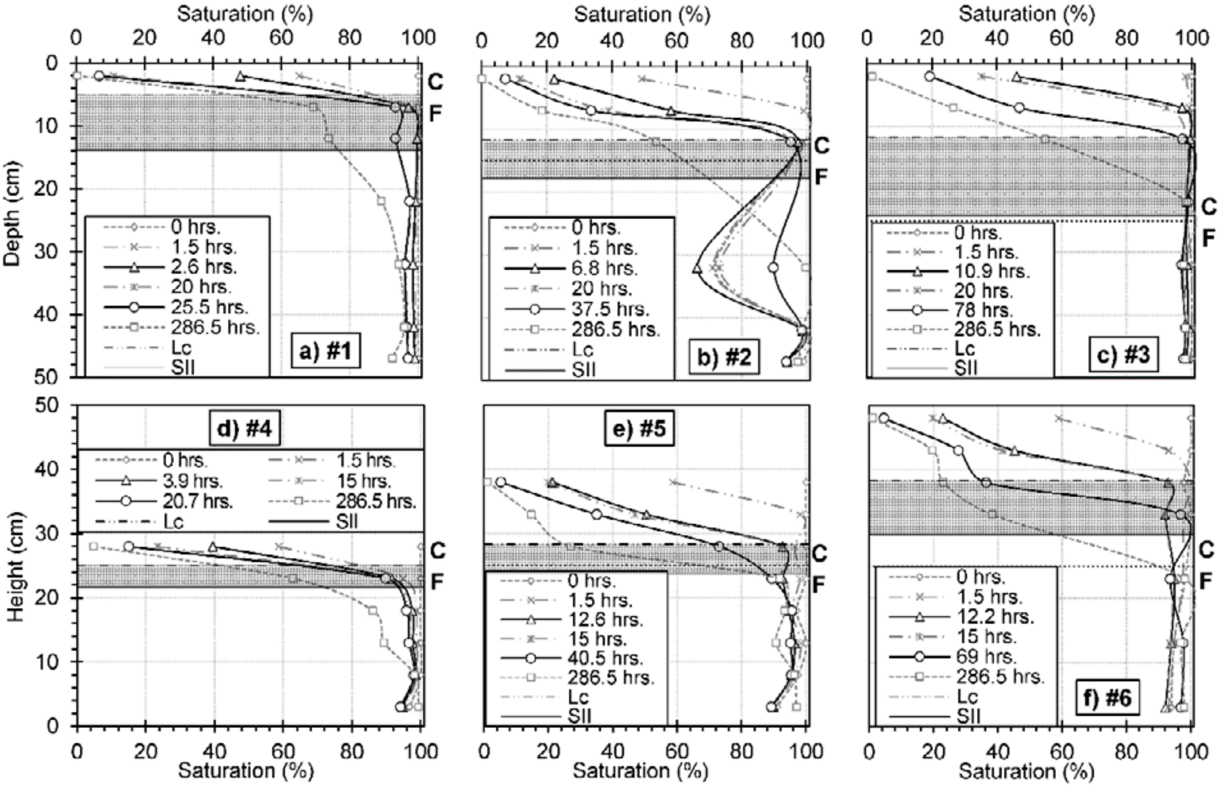

Fig. 6. Water redistribution through coarse overlying fine sand adopted configurations (groups 1 and 2). a), b) and c) show the water redistribution for group 1 adopted configurations, while d), e) and f) demonstrate group 2 adopted configurations water redistribution. SII is indicated by the region lying between the two bold curves in each figure (onset of SII and SIII respectively). In addition, the drying front depth at the end of SI (L_c) and the end of SII are also illustrated for each configuration.

For group 1, the testing duration was 286.5 hours with 2.54 mm/hr. average potential evaporation rate, average temperature of 30.98 c° and 59.63 $\%$ average relative humidity. While for group 2, test was shut down after 286.5 hours with an average potential evaporation of 3.35 mm/hr., 30.72 c° average temperature and 61.30 $\%$ average relative humidity.

Figures 5 A and B illustrate the evaporation rate versus time and evaporation rate versus drying front depth for #1, #2 and #3 (group 1) adopted configurations respectively. While **Figs. 5 C and D** demonstrate the evaporation rate versus time and evaporation rate versus drying front depth for group 2 (#4, #5 and #6) adopted configurations respectively. The potential evaporation rate from an adjacent evaporation pan subjected to the same testing conditions is shown in **Figs. 5 A and C** for group 1 and group 2 respectively. The duration and the receding drying front through SII are indicated by the intervals for each configuration as shown in **Fig. 5**.

In general, the actual evaporation rates decrease at different slopes for all adopted configurations. It can be observed that the closer the textural contrast boundary to the soil surface has the influence of decreasing the total duration required to achieve SIII, which in turn is translated into less amount of water lost through SI and SII.

#5 and #6 configurations show identical drying front depth and actual evaporation curves including SI, L_c (onset of SII), and part of SII. However, For #5, at the end of SII the actual evaporation rate reduces rapidly announcing the onset of SIII while #6 actual evaporation rate kept decreasing gradually till achieving constant and stable rate indicating the onset of SIII. This trend can be attributed to the presence of the textural contrast boundary at different depths as will be explained in the next section (Water redistribution and saturation profiles). The same trend was expected considering #2 and #3, however, the different pattern can be attributed to the lack of initial full saturation through the bottom sand layer of #2 configuration as shown in **Fig. 6 b**). However, it can be observed that #2 actual evaporation rate abruptly decreased to low and stable rate indicating the onset of SIII, while #3 evaporation rate kept decreasing gradually till achieving SIII.

In general, it can be concluded that increasing the depth of the textural contrast boundary increases the duration and the receding drying front depth through SII.

3.1.2 Water redistribution and saturation profiles

As mentioned by Shokri et al. (2010), through SI the largest capillaries of the top coarse sand layer are invaded by air while other capillaries menisci persist at the surface. Subsequently, while capillary driving forces exceed gravitational and viscous forces, menisci in the smaller capillaries would recede until only the smallest capillary remains saturated. If the vertical distance between the meniscus in the smallest and the largest capillaries of the sand layer exceeds the capillary driving force, the meniscus in the smallest capillary would retreat from the surface interrupting the continuous liquid flow and mark the onset of SII. In such a case, the drying front depth and duration of SI would not be affected by the presence of the textural boundary. However, if the thickness of the top layer is smaller than its characteristic length, the drying front would arrive to the interface between coarse and fine layers resulting in additional complexity.

Figures 6 a), b) and c) illustrate the water redistribution for group 1 adopted configurations, while **Figs. 6 d), e) and f)** demonstrate group 2 adopted configurations water redistribution. SII is indicated by the region lying between the two bold curves in each figure (onset of SII and SIII). In addition, the drying front depth at the end of SI (L_c) and the end of SII are also illustrated for each configuration.

During SI, the upper region (above the drying front, indicated by L_c) water content reduced partially as a function of the large capillaries water content. When the drying front depth exceeds the L_c, the smallest capillary meniscus starts retreating causing a dramatic reduction in the upper partially dry layer water content, while the bottom layer (below drying front) water content did not reduce significantly. Thus leads to the conclusion that through SII, lost water comes mainly from the small capillaries of the top coarse sand layer rather than the bottom fine sand layer water filled capillaries.

During SII, the drying front retreats gradually with the water molecules evaporating and diffusing through the soil body to the surface. Tracing the water redistribution through SII within the region above and below the textural contrast boundary, considering #3 and #6 configurations, the drying front retreats then was pinned within the top coarse sand layer before arriving at the textural contrast boundary. On the other hand, for #1, #2, #4 and #5 configurations, the drying front retreats till it arrives at the textural contrast boundary where it results in pining the drying front at the textural contrast boundary indicating the onset of SIII, where the top coarse sand layer small capillaries water evaporates and get lost then the air starts invading the bottom fine sand layer largest capillaries. Thus it can be concluded that the assumed linear water content distribution above the drying front is significantly affected by the textural contrast boundary. Therefore, by the end of SII, the overlying coarse sand layer had undergone extensive drying while the fine sand layer remained almost fully saturated.

As indicated in the drying front depth curves (**Figs. 5 B and D**), it can be observed that for #2, #3 and #5, #6 the characteristics length (L_c) equals to 11.7 cm (onset of SII), however for #2 and #5 configurations, the drying front at the end of SII was pinned shallower than #3 and #6 configurations where the drying front receded more within the soil profile. The pinning of the drying front for #2 and #5 is a result of the arrival of the drying front to the textural contrast boundary which announces the onset of SIII earlier than #3 and #6.

The shaded area in **Fig. 6** illustrates the severity and thickness of the desaturated zone through SII for the six adopted configurations. It must be noted that the lack of initial fully saturation of the bottom fine soil layer for configuration #2 as depicted in **Fig. 6 b)** results in a different water redistribution pattern. Where the water infiltrates with time driven by the gravitational and suction head forces from the top coarse sand layer to the underlying fine sand layer resulting in increasing the relative saturation though the bottom fine sand layer. Excluding #2 (due to the lack of initial fully saturation), it can be observed that the deeper the textural contrast boundary has the influence of increasing the thickness and severity of the desaturated zone through SII where water get lost by diffusion through the severely dried layer above the evaporation surface.

3.2 Fine overlying coarse sand profiles

3.2.1 Evaporation rate and drying front depth

Similar pattern with a reversed layering sequence as discussed in section 3.1 was adopted where six fine overlying coarse sand configurations divided into two groups were considered as mentioned in **Table 2**. Similarly, the depth of the textural contrast boundary was investigated by changing the top to the bottom layer thickness ratio [top and bottom layer thicknesses vary (#7, #8 and #9)] through group 3, while for group 4 the depth of the textural contrast boundary was investigated by changing the top fine sand layer thickness while the bottom coarse sand layer thickness maintained constant through the three adopted configurations (#10, #11 and #12). Adopted configurations were subjected to the same testing conditions within the same group.

Group 3 test was carried out for 286.5 hours with 2.45 mm/hr., 21.67 c° and 65.76 $\%$ average potential evaporation rate, average temperature and average relative humidity respectively. While group 4 test was shut down after 286.5 hours with 3.06 mm/hr., 27.89 c° and 60.36 $\%$ average potential evaporation, average temperature and average relative humidity respectively.

Evaporation rate versus time and the evaporation rate versus drying front depth for #7, #8 and #9 (group 3) adopted configurations are shown in **Figs. 7 A and B** respectively. While **Figs. 7 C and D** demonstrate the evaporation rate versus time and the evaporation rate versus drying front depth for group 4 (#10, #11 and #12) adopted configurations respectively. **Figs. 7 A and C** illustrate the potential evaporation rate for group 3 and group 4 respectively. The duration and receding drying front through SII are indicated by the intervals for each configuration as shown in **Fig. 7**.

As illustrated in **Fig. 7**, the actual evaporation rates decrease at different slopes for all adopted configurations. Similar pattern as coarse overlying fine sand configurations can be observed, where the closer the textural contrast boundary to the soil surface has the influence of significantly decreasing the total duration required to achieve SIII. Thus imposes less amount of water lost through SI and SII.

Comparing the adopted configurations through **Fig. 7**, it can be observed that the deeper the textural contrast boundary exhibits higher capability of maintaining constant actual evaporation rate (through SI) almost equal to the potential evaporation rate for longer time in comparison to the shallower textural contrast boundary adopted configurations. It must be noted that even though the δ/r ratio [boundary layer thickness to the pore size (large)] is the same for all adopted configurations in each group (same top fine sand layer material [pore size r] and same atmospheric conditions [boundary layer thickness δ]), the soil body capability of providing sufficient amount of water to the surface varies as shown in **Fig. 7**. Therefore, it can be concluded that even for the same surface material (pore size), the textural contrast boundary depth significantly affects the capability of the porous medium to supply sufficient amount of water to the surface to maintain an actual evaporation rate almost equal to the potential evaporation rate under the same conditions (high atmospheric demand).

In general, it can be concluded that increasing the depth of the textural contrast boundary increases the duration and the receding drying front depth through SII.

3.2.2 Water redistribution and saturation profiles

As mentioned in section 3.1.2, in the case where the composite characteristics length (L_c) is less than the top layer thickness, the drying front depth and duration of SI would not be affected by the presence of the textural contrast boundary. However, if the thickness of the top layer is smaller than its characteristic length, the drying front would arrive to the interface between the fine and coarse sand layers resulting in additional complexity. For fine overlying coarse sand profiles, as the meniscus in the large capillaries of the top fine sand layer arrives at the textural contrast boundary, a capillary pressure equals to

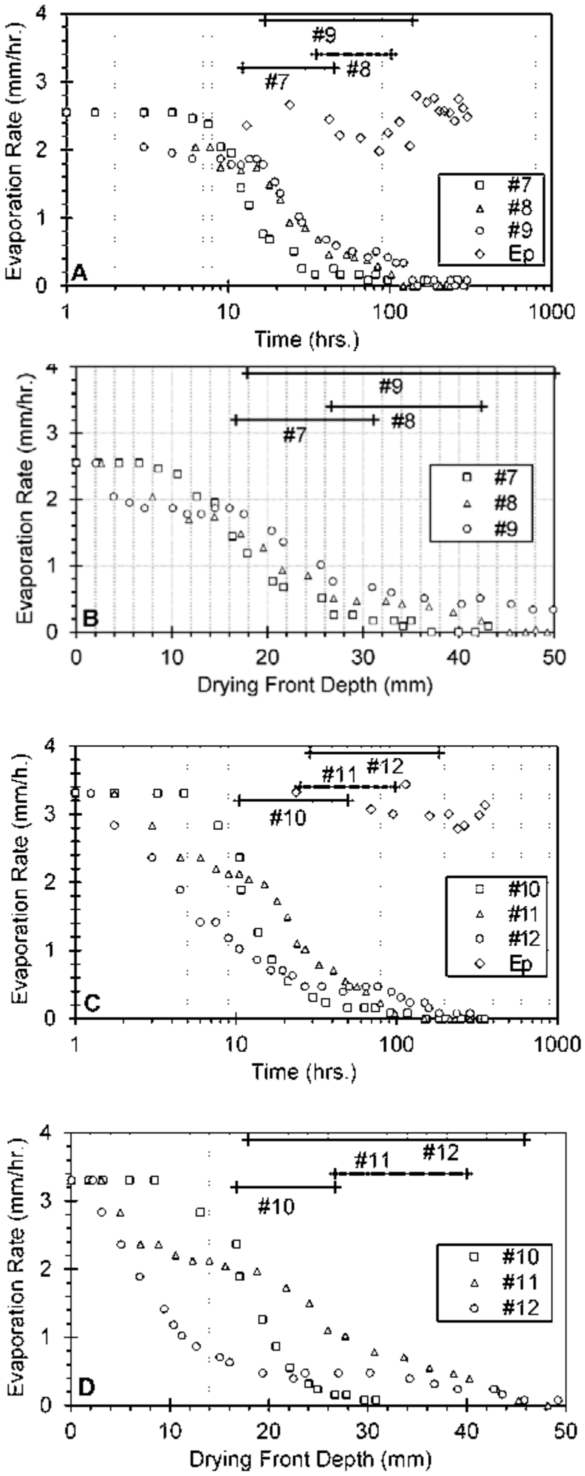

Fig. 7. Actual evaporation rates for fine overlying coarse sand adopted configurations through groups 3 and 4. A and B show the evaporation rate versus time and drying front depth for group 3 (#7, #8 and #9 adopted configurations) respectively. C and D demonstrate the evaporation rate versus time and drying front depth for group 4 (#10, #11 and #12 adopted configurations) respectively. The potential evaporation rate obtained by an evaporation pan placed adjacent to the soil columns and subjected to the same testing conditions is also shown in Figs. A and C.

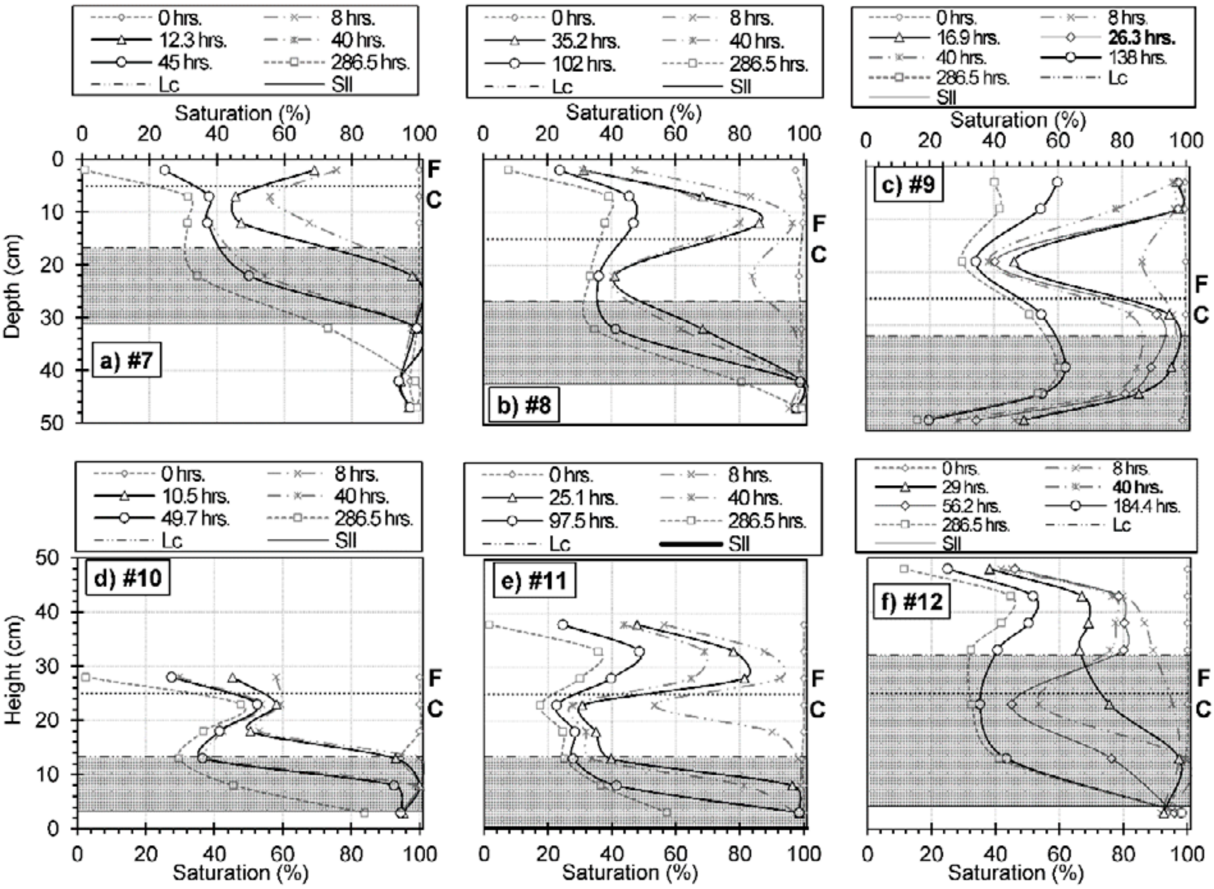

Fig. 8. Water redistribution through fine overlying coarse sand adopted configurations (groups 3 and 4). a), b) and c) show the water redistribution for group 3 adopted configurations, while d), e) and f) demonstrate group 4 adopted configurations water redistribution. SII is indicated by the region lying between the two bold curves in each figure (onset of SII and SIII respectively). In addition, the drying front depth at the end of SI (L_c) and the end of SII are also illustrated for each configuration.

the air entry value of the fine layer is introduced to the underlying coarse sand layer. This value might be larger than the pressure required for invading the largest capillary of bottom coarse sand layer. The abrupt introduction of such excess capillary pressure (nominally expressed as the difference between air entry values of fine and coarse sand layers) induces rapid and disproportional displacement of water molecules. Consequently, in order to dissipate the imposed energy and relax the pressure perturbation relative to the evaporation rate, water ejection from bottom coarse sand layer to the overlying fine sand layer occurs (Shokri et al., 2010).

Figures 8 a), b) and c) show the water redistribution for group 3 adopted configurations, while **Figs. 8 d), e) and f)** demonstrate group 4 adopted configurations water redistribution. SII is indicated by the region lying between the two bold curves in each figure (onset of SII and SIII). In addition, the drying front depth at the end of SI (L_c) and the end of SII are also illustrated.

As demonstrated in **Fig. 8**, the L_c exceeds the textural contrast boundary for #7, #8 and #10, #11 configurations. Therefore, the pumping phenomenon occurs causing ejecting the water from the bottom coarse sand layer to the top fine sand layer through SI. As mentioned by Shokri et al. (2010), the amount of applied capillary pressure equals the difference between the air entry values of the bottom and top layers. Since the same material is used for all adopted configurations, the amount of developed pressure introduced to the bottom coarse sand layer is the same for all the adopted configurations. This hypothesis can be confirmed by tracing the drying front where it was pinned at the same distance (depth) from the textural contrast boundary indicating the onset of SIII.

It can be concluded that for fine overlying coarse soil profiles with L_c larger than the top fine sand layer thickness, the end of SII is defined by dissipating all the introduced capillary pressure from the top fine soil layer to the bottom coarse sand layer.

Considering #9 and #12 configurations as illustrated in **Figs. 8 c) and f)**, the L_c is less than the textural contrast boundary depth for both configurations. However, it can be observed that the bottom coarse sand layer water content started decreasing even before the drying front reaches the textural contrast boundary. Thus leads to the fact that even for the case where L_c is less than the textural contrast boundary depth, the pumping phenomenon from the bottom coarse sand layer to the top fine sand layer does occur. This can be attributed to the increasing suction forces (water decreasing) within the top fine sand layer which develops a driving force pulling the water through the connected capillaries between the top and bottom sand layers. Through this stage where the drying front is shallower than the textural contrast boundary, the water content within the top fine sand layer remains higher than the bottom coarse sand layer water content.

However, after the drying front reaches the textural contrast boundary, the pumping phenomenon due to the introduced capillary pressure defined by Shokri et al. (2010) enhances ejecting the water from the bottom coarse sand layer to the top fine sand layer resulting in a water redistribution as illustrated in **Figs. 8 c) and f)** (top layer water content is higher than the bottom layer). Therefore, at the end of the test where the drying front depth retreats below the textural contrast boundary, the whole soil profile (top and bottom sand layers) has undergone extensive drying.

The severity and thickness of the desaturated zone through SII for the six adopted configurations is illustrated in **Fig. 8** by the shaded area. It can be observed that the deeper the textural contrast boundary has the influence of significantly increasing the thickness and severity of the desaturated zone through SII where water get lost by diffusion through the severely dried layer above the evaporation surface.

3.3 Water storage capability

After the continuous hydraulic connection between the drying front and the evaporation surface breaks, SII starts where the smallest capillaries menisci retreat displacing the evaporation surface deeper below the soil surface with time. Therefore, in order to evaluate the textural contrast boundary influence on the amount of water lost through SII, the ratio between the top to the bottom layer residual water content [θ_r (representing the smallest capillary)] multiplied by the top to the bottom layer thickness is plotted against the reduction in the degree of saturation within SII through the whole soil profile is illustrated in **Fig. 9**. It can be observed that small ratio configurations impose higher water storage capability through SII, where the water content reduction is very small compared to the large ratios where a significant drop in the saturation was observed.

Finally, regardless the atmospheric conditions, it can be concluded that for both coarse overlying fine and fine overlying coarse sand profiles, the shallower the textural contrast boundary imposes higher water storage capabilities through SI and SII.

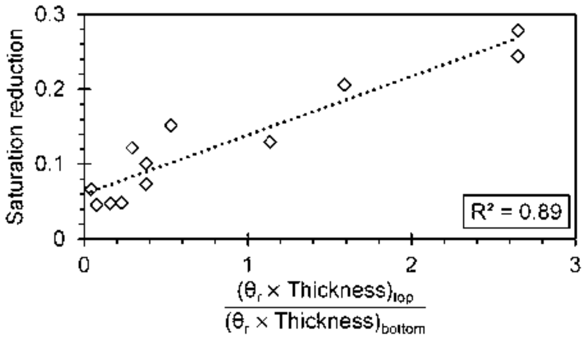

Fig. 9. Water storage capability. The textural contrast boundary depth influence on the soil profile water storage capability is demonstrated by plotting the ratio between the top to the bottom layer residual water content [θ_r (smallest capillary)] multiplied by the top to the bottom layer thickness against the reduction in the degree of saturation through the entire soil profile at the end of SII.

4. Conclusions

The textural contrast boundary depth, individual layer thickness and layering sequence influence on the actual evaporation rate and the water storage through double-layered soil profiles were investigate through 12 adopted double layered soil configurations. In general, the closer the textural contrast boundary to the soil surface has the influence of decreasing the total duration required to achieve SIII, which in turn is translated into less amount of water lost through SI and SII. In addition, it was observed that the deeper the textural contrast boundary has the influence of significantly increasing the thickness and severity of the desaturated zone through SII where water get lost by diffusion through the severely dried layer above the evaporation surface.

For coarse overlying fine soil profiles, it was observed that the small capillaries of the top coarse sand layer contributed to the majority of the lost water through SII. While the bottom layer capillaries remained almost filled till the end of SII. It must be noted that the linearity of water content profile above the drying front is significantly affected by the presence and depth of the textural contrast boundary. Therefore, at the end of the experiment, the overlying coarse sand layer had undergone extensive drying while the fine sand layer maintained high degree of saturation.

For fine overlying coarse soil profiles, even when the same surface material is used (large δ/r ratio) under the same atmospheric conditions, the textural contrast boundary depth significantly affects the capability of the porous medium to supply sufficient amount of water to the surface to maintain an actual evaporation rate almost equal to the potential evaporation rate during SI. For the case where L_c is less than the textural contrast boundary depth, through the stages where the drying front is shallower than the textural contrast boundary the pumping phenomenon from the bottom coarse sand layer to the top fine sand layer does occur. This phenomenon can be attributed to the increasing suction forces within the top fine sand layer which develops a driving force pulling the water through the connected capillaries between the top and bottom sand layers. Through those stages, the water content within the top fine sand layer remains higher than the bottom coarse sand layer water content. However, after the drying front reaches the textural contrast boundary, the pumping phenomenon due to the introduced capillary pressure enhances ejecting the water from the bottom coarse sand layer to the top fine sand layer. In addition, for soil profiles with L_c larger than the top fine sand layer thickness, the end of SII is defined by dissipating all the introduced capillary pressure from the top fine soil layer to the bottom coarse sand layer.

Regardless the layering sequence it was observed that small top to bottom layer residual water content multiplied by the top to the bottom layer thickness ratio configurations impose higher water storage capability through SII, where the water content reduction is very small in comparison to the large ratios where a significant drop in the degree of saturation was observed. Finally, regardless the atmospheric conditions it can be concluded that for both coarse overlying fine and fine overlying coarse sand profiles, the shallower the textural contrast boundary imposes higher water storage capabilities through SI and SII.

Acknowledgements

The authors express their gratitude to Assoc. Professor Ryohei Ishikura and the laboratory technical assistant Mr. Michio Nakashima for their great support.

References

Aubertin, M., Bussière, B., Chapuis, R.D. and Barbera, J., 1996. Construction of experimental cells with covers on acid producing tailings. Proc. 49th Canadian Geotechnical Conference, September 23-September 25, 2014, Montreal, Canada: 655–662.

Blight, G.E., 2002. Measuring evaporation from soil surfaces for environmental and geotechnical purposes. Water SA, **28** (4): 381-394.

Blight, G.E., 2003. The vadose zone soil-water balance and transpiration rates of vegetation. Geotechnique, **53** (1): 55-64.

Brutsaert, W. and Chen, D., 1995. Desorption and the two stages of drying of natural tallgrass prairie. Water Resources Research, **31** (5): 1305-1313.

Brutsaert, W., 2005. Hydrology: An Introduction. Cambridge University Press, New York: pp 618.

Diaz, F., Jimenez, C.C. and Tejedor, M., 2005. Influence of the thickness and grain size of tephra mulch on soil water evaporation. Agricultural Water Management, **74** (1): 47-55.

Fisher, E.A., 1923. Some factors affecting the evaporation of water from soil. The Journal of Agricultural Science, **13** (02): 121-143.

Gillette, D.A., Niemeyer, T.C. and Helm, P.J., 2001. Supply limited horizontal sand drift at an ephemerally crusted, un-vegetated saline playa. Journal of Geophysical Research: Atmospheres, **106** (D16): 18085-18098.

Huang, M., Bruch, P.G. and Barbour, S.L., 2013. Evaporation and water redistribution in layered unsaturated soil profiles. Vadose Zone Journal, **12** (1).

JIS, A., 1224 Standard, 2009. Test Method for Minimum and Maximum Densities of Sands, Japanese Geotechnical Society.

Lehmann, P., Assouline, S. and Or, D., 2008. Characteristic lengths affecting evaporative drying of porous media. Physical Review E, **77** (5): 056309.

Murakami, S., Yasuhara, K. and Mochizuki, N., 2002. An observational prediction of land subsidence for a GIS-aided monitoring system of groundwater level. Lowl Technol Int, **4** (1): 46-61.

Pillai, K.M., Prat, M. and Marcoux, M., 2009. A study on slow evaporation of liquids in a dual-porosity porous medium using square network model. International Journal of Heat and Mass Transfer, **52** (7): 1643-1656.

Prat, M., 2002. Recent advances in pore-scale models for drying of porous media. Chemical Engineering Journal, **86** (1): 153-164.

Schlünder, E.U., 1988. On the mechanism of the constant drying rate period and its relevance to diffusion controlled catalytic gas phase reactions. Chemical Engineering Science, **43** (10): 2685-2688.

Seki, K., 2007. SWRC fit? a nonlinear fitting program with a water retention curve for soils having unimodal and bimodal pore structure. Hydrology and Earth System Sciences Discussions, **4** (1): 407-437.

Shahraeeni, E., Lehmann, P. and Or, D., 2012. Coupling of evaporative fluxes from drying porous surfaces with air boundary layer: Characteristics of Evaporation from Discrete Pores. Water Resources Research, **48** (9).

Shokri, N., Lehmann, P. and Or, D., 2010. Evaporation from layered porous media. Journal of Geophysical Research: Solid Earth, **115** (B6).

Shokri, N., Lehmann, P., Vontobel, P. and Or, D., 2008. Drying front and water content dynamics during evaporation from sand delineated by neutron radiography. Water Resources Research, **44** (6).

Schwartz, J., 1994. Air pollution and daily mortality: a review and meta-analysis. Environmental research, **64** (1): 36-52.

Teng, J., Yasufuku, N., Liu, Q. and Liu, S., 2014. Experimental evaluation and parameterization of evaporation from soil surface. Natural Hazards, **73** (3): 1405-1418.

Van Brakel, J., 1980. Mass transfer in convective drying. Advances in Drying, volume 1: pp 212–267.

Van Genuchten, M.T., 1980. A closed-form equation for predicting the hydraulic conductivity of unsaturated soils. Soil Science Society of America Journal, **44** (5): 892-898.

Wilson, G.W., Fredlund, D.G. and Barbour, S.L., 1994. Coupled soil-atmosphere modelling for soil evaporation. Canadian Geotechnical Journal, **31** (2): 151-161.

Yanful, E.K., Bell, A.V. and Woyshner, M.R., 1993. Design of a composite soil cover for an experimental waste rock pile near Newcastle, New Brunswick, Canada. Canadian Geotechnical Journal, **30** (4): 578-587.

Yanful, E.K., Mousavi, S.M. and Yang, M., 2003. Modeling and measurement of evaporation in moisture-retaining soil covers. Advances in Environmental Research, **7** (4): 783-801.

Yiotis, A.G., Tsimpanogiannis, I.N., Stubos, A.K. and Yortsos, Y.C., 2006. Pore-network study of the characteristic periods in the drying of porous materials. Journal of Colloid and Interface Science, **297** (2): 738-748.

Symbols and abbreviations

GS	Specific gravity
ρ_s	Soil dry density
Uc	Uniformity coefficient
Uc`	Curvature coefficient
D50	Median diameter
k_s	Saturated hydraulic conductivity
θ_r	Residual volumetric water content
θ_s	Saturated volumetric water content
σ	Water-air surface tension
ρ	Water density
g	Acceleration of gravity
r	Capillary radius
r_1	Smallest drainable pore
r_2	Largest drainable pore
Δh_{cap}	Capillary head difference
h_b	Air entry value
α	Van Genuchten fitting parameter, related to the inverse of the air entry value
n	Van Genuchten fitting parameter, measure of the pore-size distribution
L_c	(composite) Characteristic length
L_i	Individual layer characteristic length
Z_i	Individual layer thickness
h_{ri}	Suction at residual water content
ϕ	Porosity
δ	Boundary layer thickness (air)